IMPROVED LIMITS ON THE WEAK, NEUTRAL, HADRONIC AXIAL VECTOR COUPLING CONSTANTS FROM QUASIELASTIC SCATTERING OF POLARIZED ELECTRONS

W. HEIL[1], J. AHRENS[3], H.G. ANDRESEN[1], A. BORNHEIMER[1], D. CONRATH[2], K.-J. DIETZ[2], W. GASTEYER[2], H.-J. GESSINGER[2], W. HARTMANN[2], J. JETHWA[4], H.-J. KLUGE[2], H. KESSLER[2], T. KETTNER[1], L. KOCH[2], F. NEUGEBAUER[2], R. NEUHAUSEN[1], E.W. OTTEN[2], E. REICHERT[2], F.P. SCHÄFER[4] and B. WAGNER[1]

[1] *Institut für Kernphysik der Universität Mainz, D-6500 Mainz, FRG*
[2] *Institut für Physik der Universität Mainz, D-6500 Mainz, FRG*
[3] *Max-Planck-Institut für Chemie, Abt. Kernphysik, D-6500 Mainz, FRG*
[4] *Max-Planck-Institut für biophysikalische Chemie, D-3400 Göttingen, FRG*

In scattering polarized electrons ($P_1 = 44\%$) by ^{9}Be at an energy of 300 MeV at angles $115° \leqslant \vartheta \leqslant 145°$ a parity violating asymmetry of $\overline{A}_{\text{corr}} = (-3.5 \pm 0.7 \pm 0.2) \times 10^{-6}$ was measured. After correction for finite electron polarization and background we deduce an experimental asymmetry of $A_{\text{ex}} = (-9.4 \pm 1.8 \pm 0.5) \times 10^{-6}$. The quoted errors indicate the statistical and the systematic uncertainties, respectively. The asymmetry, which is dominated by the quasielastic cross section, is interpreted in terms of model-independent electron–nucleon coupling constants of the weak neutral current. The error limits in the sector of axial vector coupling constants have been improved by a factor of 3 over previous results. A model-dependent analysis for the Weinberg angle yields the result $\sin^2 \theta_W = 0.221 \pm 0.014 \pm 0.004$.

1. Introduction

The era of experiments on the electroweak interaction started in 1973 with the discovery of neutral weak currents at CERN [1] and culminated when the carriers of this interaction, the heavy bosons W^+, W^-, Z^0 were produced and detected at the CERN p̄p collider [2]. All experiments performed in this field, including those in atomic physics at very low energies, are in accordance with the standard model of Glashow, Weinberg and Salam [3]. It contains a free parameter, the Weinberg angle, to be fixed by experiment. Its best value is $\sin^2 \theta_W = 0.223 \pm 0.004$ [4]. The generality and unambiguity of the GWS theory should be tested by experiments at various energies and between particles of all kinds. Included here are experiments at low and intermediate energies, for which Hung and Sakurai have formulated a general form of the neutral weak interaction, based on an effective point-like vector–axial vector (V, A) coupling [5]. It contains free parameters to be fixed by experiment.

At energies far below the Z^0 mass, the neutral weak interaction between charged particles can only be detected by its parity violating (PV) asymmetry. This quality discriminates against the competing parity conserving electromagnetic interaction which otherwise dominates by many orders of magnitude. In the electron–hadron sector, which is of interest for our experiment, the parity violating part of the neutral weak current is given by [6]

$$L_{PV}^{eH} = -\frac{G_F}{\sqrt{2}} \left\{ A_\mu^{e^-} \left(\tilde{\alpha} V_{IV}^\mu + \tilde{\gamma} V_{IS}^\mu \right) + V_\mu^{e^-} \left(\tilde{\beta} A_{IV}^\mu + \tilde{\delta} A_{IS}^\mu \right) \right\}. \tag{1}$$

$A_\mu^{e^-}, V_\mu^{e^-}$ denote the axial vector and vector current of the electron, respectively; the corresponding hadronic currents are split into isovector (V_{IV}^μ, A_{IV}^μ) and isoscalar components (V_{IS}^μ, A_{IS}^μ). G_F is the Fermi coupling constant. $\tilde{\alpha}, \tilde{\gamma}$ and $\tilde{\beta}, \tilde{\delta}$ are free parameters to be determined by experiment. Parity violating asymmetries have been observed in the scattering of polarized electrons from deuterons at high energies at SLAC [7] and in spectra of heavy atoms at very low energies [8]. Both types of experiments were sensitive mainly to the hadronic vector current with almost orthogonally linear combinations of $\tilde{\alpha}$ and $\tilde{\gamma}$. Thus this pair of coupling constants could be determined model-independently from these experiments to be [4]

$$\tilde{\alpha} = -0.65 \pm 0.16, \qquad \tilde{\gamma} = 0.143 \pm 0.0175. \tag{2}$$

Contributions from the hadronic axial vector current were too small to yield significant values for the corresponding coupling constants $\tilde{\beta}$ and $\tilde{\delta}$.

In contrast to the SLAC experiment, the kinematical conditions in scattering electrons of medium energy at backward angles from nuclei enhance the sensitivity to the hadronic axial vector current, at which our experiment was aimed. We report in this paper the measurement of the PV asymmetry in inclusive scattering of polarized electrons by ^{9}Be at an energy $E_0 = 300$ MeV at an average angle $\bar{\vartheta} = 130°$ where the cross section is dominated by quasi-elastic scattering. For these conditions (including the response function of the detector) the asymmetry has been calculated in terms of the coupling constants to be

$$A_{PV} = \frac{\sigma^+ - \sigma^-}{\sigma^+ + \sigma^-} = \left(1.69\tilde{\alpha} + 2.11\tilde{\beta} + 1.04\tilde{\gamma} + 0.08\tilde{\delta} \right) \times 10^{-5}, \tag{3}$$

where σ^+ (σ^-) are the cross sections for positive (negative) electron helicity (see appendix A). In eq. (3) $\tilde{\beta}$ has the highest weight, whereas the contribution of $\tilde{\delta}$ remains small. The enhanced sensitivity to $\tilde{\beta}$ has been bought at a very high price: due to the smaller momentum transfer, the asymmetry (3) has dropped to the level of 10^{-5}, a factor of 10 smaller than observed in the SLAC experiment. Thus the problems of increasing statistical accuracy and suppressing systematic errors to satisfactory levels are drastically increased.

The asymmetry (3) has been calculated on the basis of a paper by Hoffmann and Reya [9]. They treat the electroweak electron–nucleon scattering in terms of the elastic nucleon form factors which are experimentally known from electron scattering and neutrino reactions. In this respect the analysis differs from the one used in the high-energy experiment [10] which was based on the model of asymptotically free quarks. The extension of Hoffmann and Reya's theory to quasi-elastic scattering has been given in ref. [11] and is briefly sketched in appendix A, where corrections from competing processes are also discussed.

In sect. 2 we explain the experimental set-up and procedure. Part of the equipment has been developed especially for this experiment and will be described in detail in separate publications [12–15]. Sect. 3 deals with the data taking and sect. 4 with the data analysis. The discussion of the results is given in sect. 5, followed by conclusions (sect. 6) and appendices A.1–A.4.

2. Experimental set-up and procedure

2.1. GENERAL CONSIDERATIONS AND LAYOUT

The experimental procedure is completely dictated by the demand to achieve statistical and systematic errors smaller than 10^{-6} for the measured asymmetry. Thus a number of $N > 10^{12}$ scattering events is required which should be registered within a typical running time of one week. Considering a duty factor of $\approx 1.5 \times 10^{-4}$ of the accelerator, the event rate during a pulse will be about $10^{10}/s$ which cannot be handled on the basis of individual event counting. Instead, the signal has to be integrated by analog circuits. Thus one is deprived of any electronic means of separating true events from the background. Assuming a cross section $d\sigma/d\Omega \simeq 10^{-31}$ cm^2/sr for ^{9}Be and a target thickness of 10^{23} atoms/cm^2 one obtains a design figure for the product of the peak current (I_P) and the solid angle ($\Delta\Omega$) of detection of $I_P \cdot \Delta\Omega = 100$ mA $\cdot$ sr. Considering the limits on I_P ($I_P \leqslant 100$ mA) one aimed at a solid angle $\Delta\Omega > 1$ sr. This demand excluded the use of conventional magnetic spectrometers. A satisfactory solution was found by using an array of imaging gas Čerenkov counters. These are shown in fig. 1 together with the general layout of the experiment, which is described in the following.

The source for longitudinally polarized electrons is a GaAsP photocathode, irradiated by circularly polarized laser light. A magnet deflects the beam into the 300 MeV Linac, or alternatively into an analyzer, consisting of a Wien filter (WF), which rotates the spin by 90°, and a Mott scattering chamber (MD) [16]. An energy compressing system at the end of the Linac provides an energy spread $\delta E/E \approx 0.1\%$. The achromatic magnet M1 bends the beam by 90°. This produces a spin rotation at 300 MeV of 151° due to the relativistic enhancement of the g-factor anomaly by the γ-factor. At that stage the polarization can be measured by Møller scattering (MP) from a magnetized Fe target. The two Møller electrons emerge from the axis
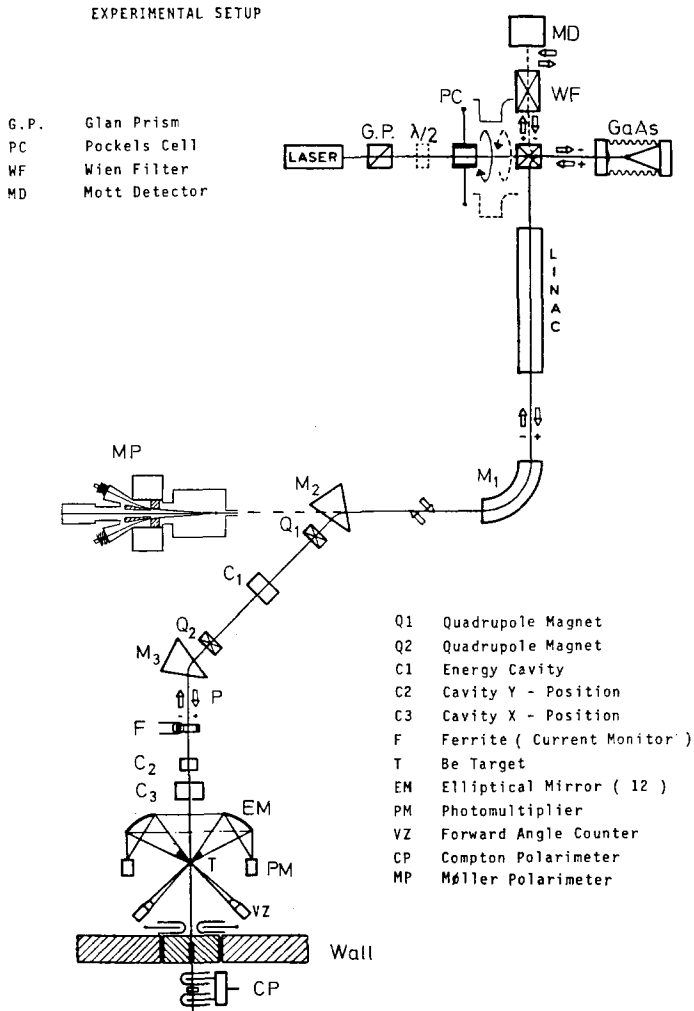
EXPERIMENTAL SETUP

G.P.   Glan Prism
PC   Pockels Cell
WF   Wien Filter
MD   Mott Detector

Q1   Quadrupole Magnet
Q2   Quadrupole Magnet
C1   Energy Cavity
C2   Cavity Y - Position
C3   Cavity X - Position
F   Ferrite (Current Monitor)
T   Be Target
EM   Elliptical Mirror (12)
PM   Photomultiplier
VZ   Forward Angle Counter
CP   Compton Polarimeter
MP   Møller Polarimeter

Fig. 1. Overall arrangement of the Mainz parity violation experiment.

of a quadrupole magnet at an angle of $\pm 3.3°$ and are bent off axis by the quadrupole field onto two detectors in coincidence. Different orientations of the magnetized foil allow separate measurements of longitudinal and transverse polarization components. They are plotted in fig. 2 as a function of the beam energy, showing their rotation with respect to the beam axis.

The achromatic doublet (M2, M3) bends the beam back into the original direction and thus restores the longitudinal polarization. A position sensitive microwave cavity (C1) [17] is placed in the energy dispersive symmetry plane of this achromate. It senses any deviation of the center of gravity of the beam position on a
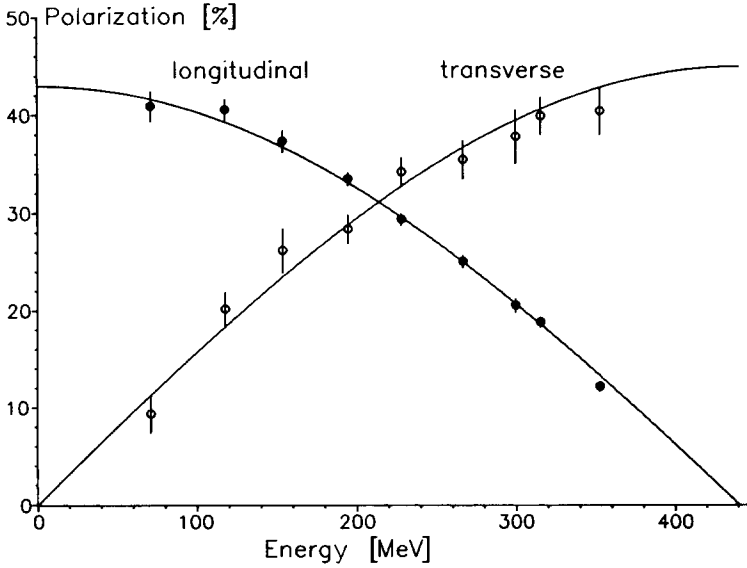
Fig. 2. Longitudinal and transverse polarization components as functions of the beam energy measured by the Møller polarimeter after 90° beam bending [13]. The solid lines correspond to calculated values.

pulse-to-pulse basis with a sensitivity of about 5 μm. With the dispersion being 0.4 MeV/mm at this point, one achieves a resolution of 2 keV in measuring variations of the mean energy. Two additional cavities of this kind (C2, C3) monitor the x- and y-position of the beam in front of the target.

A Rogowski coil (F) in front of the target integrates the beam current of individual pulses in order to normalize the scattered intensity with respect to the incoming one. Supplementary beam control is provided by 4 forward detectors (VC) (lucite Čerenkov detectors). They are mounted symmetrically at a scattering angle of 15° where the momentum transfer is too small to cause a significant PV asymmetry. Since they measure the product of beam intensity times target thickness, they can also serve for normalizing the scattered intensity. Moreover, they are sensitive to changes of beam position and energy.

On line control of the longitudinal polarization is provided by a Compton polarimeter. It is placed behind the beam dump, where the circular polarization of the bremsstrahlung photons from the ^{9}Be target can be measured, which is directly related to the polarization degree of the traversing electron beam. It consists of two ionization chambers, separated by a magnetized Compton absorber (see fig. 6). The instrument is calibrated by comparing to measurements with the Møller polarimeter at the beginning and the end of each run. Its analyzing power defined by

$$a = \frac{1}{P_{c,\ell}} \cdot A_R \quad \text{with} \quad A_R = \frac{R^+ - R^-}{R^+ + R^-} \tag{4}$$

has thus been measured to be $a = 2 \times 10^{-3}$. $P_{e,\ell}$ is the longitudinal electron polarization and R^+, R^- are the ratios of ionization currents in the two chambers for positive and negative helicity, respectively.

Forthcoming papers will deal with details of the construction and performance of the polarized electron source [12], of the Møller polarimeter [13], of the Compton polarimeter [14], and of the Čerenkov detector [15]. Nevertheless, it is necessary to describe in the following the most important features of the polarized source and the Čerenkov detector in order to enable a thorough discussion of the measurements and their analysis.

2.2. POLARIZED ELECTRON SOURCE

We have chosen a GaAsP photo-electron source which was designed following the layout of the SLAC source [18]. Due to the much lower PV asymmetry expected in this experiment, the demands concerning life-time, pulse shape and emission asymmetry were substantially higher, however. A schematic drawing of the source, its optics and electronics is shown in fig. 3a. The flash bulb driven dye laser was built at the Max-Planck-Institut für biophysikalische Chemie at Göttingen [19] and was specially adapted to the needs of this experiment. It delivers pulses of about 20 mJ with a halfwidth of 5 to 6 μs at a repetition rate of 50 Hz. The wavelength was tuned to 643 nm by dissolving the dye (sulforhodamin B) in Ammonyx solution (4%) at a concentration of 2×10^{-4} mol/liter. With a stock of 70 liter of dye solution the laser power could be kept for about 24 h at the level mentioned above. Thereafter, the dye and the flash bulbs of the laser were replaced.

After passing several optical elements for pulse shaping and circularly polarizing, the laser beam was focussed on a $GaAs_{1-x}P_x$ crystal with a phosphoric content of $x = 38\%$. The surface was covered by a CsF layer providing negative electron affinity. Depending on the history of crystal preparation and running conditions the electron emission ranged between 1.7 and 5 mA per Watt laser power incident onto the cathode. The source was run at room temperature and a vacuum of about 3×10^{-10} mbar. Under these conditions the source could be operated for typical running times of 100 h without intermediate retreatment of the cathode surface.

At optimum emission the electron polarization ranged between 42 and 50%. Fig. 4 shows $P_{e,\ell}$ as measured by the Compton polarimeter during the two production runs (May and November 1986). The sharp rise of $P_{e,\ell}$ in the middle of the May run is correlated with a decrease of emission which was probably caused by a transient vacuum problem [20].

Satisfactory accelerator operation requires rectangular electron pulses with a top flatness and amplitude stability of better than 1%. For this purpose a pulse-shaping optical device, consisting of a transverse Pockels cell (MOD) between two Glan–Thomson polarizers (GT) is introduced into the laser beam (see fig. 3a). The transmission of this device is controlled by the voltage-dependent birefringence of
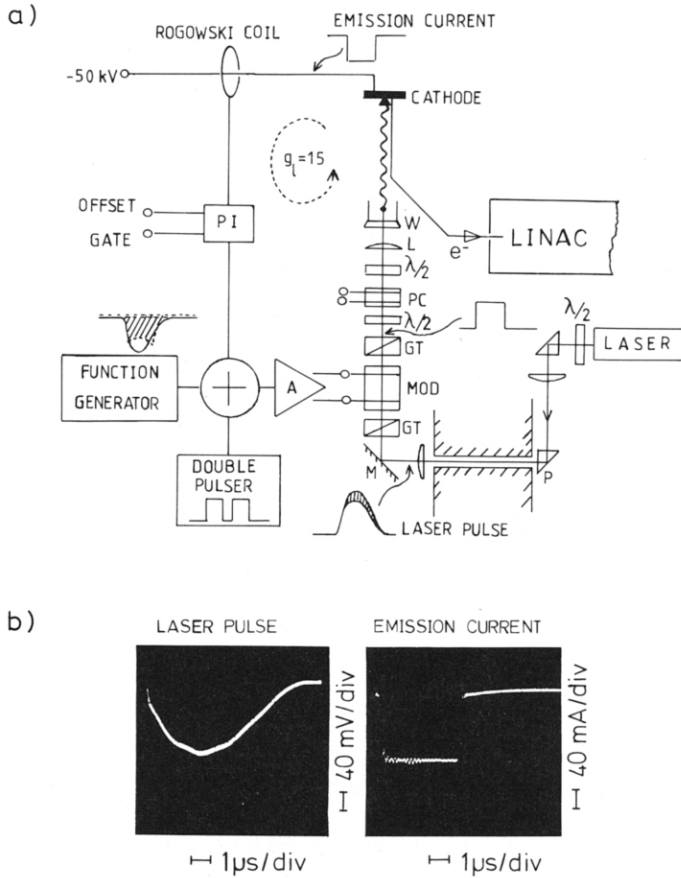
a)

b)

Fig. 3. (a) Schematic drawing of the GaAsP source and its optics together with the block diagram of the forward and feedback control: A = amplifier, PI = filter, GT = Glan–Thomson prism, L = lens, $\lambda/2$ plate, M = mirror, MOD = transverse Pockels cell, PC = Pockels cell, P = prism, W = vacuum window. (b) Oscillograms of the original laser pulse and the final emission pulse shaped and intensity-stabilized by electro-optic control.

the Pockels cell which is driven by two additive control circuits. The first one is a forward regulation which preshapes the laser pulse by a suitably shaped input signal from a function generator. The second is a fast feedback loop with a bandwidth of about 10 MHz and a loop amplification of 15. It connects directly to the emission current which is picked up by a Rogowski coil. This signal is compared with a standard pulse and the difference used as a control signal. Since the pulse-to-pulse fluctuation of the laser power was of the order of 1%, one achieved, with the amplification as given, a short-term stability of the height of the emission pulse of typically 0.1% whereas the flatness reached the desired value of 1%. Fig. 3b shows oscillograms of the original laser pulse and the final emission pulse of 3.5 μs length
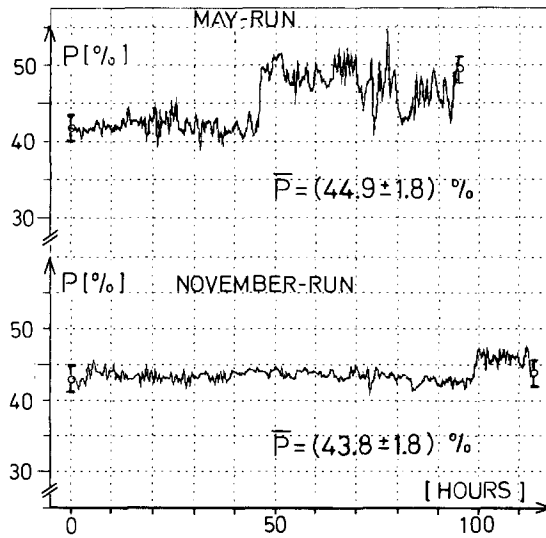
Fig. 4. On-line control of the beam polarization at the target position by the Compton polarimeter, which was calibrated at the beginning and the end of each run by means of the Møller polarimeter. The results of the Møller scattering experiments are indicated by the circles with error bars.

and typically 140 mA height. Taking into account the duty cycle and a total transmission of $\approx 30\%$, one arrives at an average current of about $7\,\mu A$ as delivered to the target.

The laser light was circularly polarized either right- or left-handed ($+$ or $-$) by applying the corresponding voltage to another Pockels cell (PC in fig. 3a). The polarization of every second beam pulse was randomly chosen but the following pulse was set to the opposite polarization. In this way, influences of drifts of the set-up could be minimized by calculating single asymmetries (A_s) from these pairs of ordered, consecutive beam pulses.

A slow cycle was superimposed onto this fast cycle by turning mechanically the $\lambda/2$ plate between the second Glan–Thomson prism and the second Pockels cell (PC) by $45°$ every 15 min (see fig. 3a). By this procedure the sign of polarization (produced by the electronic signals fed to the Pockels cell) was interchanged and hence it was possible to eliminate any possible electronic cross talk of these high voltage signals to the data taking system which might cause a fake asymmetry. We refer to these 15 min subruns as $\lambda/2^+$ or $\lambda/2^-$ runs.

It was of utmost importance for this experiment that we succeeded in minimizing the correlation between the sign of polarization and the beam intensity (I_e) to a level of 10^{-5}. Although this correlation cancels to first order in the asymmetry of normalized scattering signals, this very stringent requirement had to be met because we observed a background from the halo of the accelerator beam. This background

exhibited a strong and uncontrollable correlation to intensity variations (see subsect. 4.2). The problem could not be solved by aiming for perfect right- and left-handed polarization of the laser beam with identical intensities, beam spots, etc. Such attempts resulted in significant emission asymmetries of $A_e > 10^{-3}$ (with open feed-back loop), because the slightest birefringence (e.g. of the vacuum window) followed by some polarizing element will destroy the left–right symmetry of the intensities. On the contrary, it was necessary to compensate these effects by an asymmetric input, i.e. the polarizations were chosen to be slightly elliptical and different for $+$ and $-$. Moreover, the axis of the ellipse was rotated by another $\lambda/2$-plate in order to find a minimum of A_e. With these additional parameters one could find a condition for which A_e was minimized simultaneously for the $\lambda/2^+$ and $\lambda/2^-$ runs down to the level of 10^{-5}. This value includes the reduction factor

TABLE 1

Parameters of the two production runs and experimental asymmetries

Line	Run May 1986		Run Nov. 1986	
1 Averaged beam current at target position	6.9 μA		7.5 μA	
2 S/B ratio	5.02		5.19	
3 Polarization (%)	44.9 $\pm$ 1.8		43.8 $\pm$ 1.8	
4 Position of $\lambda/2$ plate	$+$	$-$	$+$	$-$
5 Number of 15 min runs	191	182	225	225
6 $\langle x^+ - x^- \rangle$ (μm)	$+1.01$	-0.38	$+0.78$	-0.44
7 $\langle y^+ - y^- \rangle$ (μm)	$+0.52$	-0.18	$+0.37$	-0.21
8 $\langle E^+ - E^- \rangle$ (keV)	$+0.7$	-0.27	-0.31	$+0.20$
9 A_e (emission)	-22.1 ± 2.4	2.0 ± 2.5	6.3 ± 2.4	5.7 ± 2.2
10 A_1 (ferrit)	-2.0 ± 3.2	1.2 ± 3.2	-6.4 ± 2.3	0.3 ± 2.3
11 A^f (electronic)	< 0.08		< 0.08	
12 A^f_{Mott}	< 0.04		< 0.04	
13 $A^f_{Møller}$	< 0.08		< 0.08	
14 A^f_n	$< 10^{-2} A_l$		$< 10^{-2} A_l$	
15 A^f_p (x-cavity)	-1.60 ± 0.82	-0.16 ± 0.49	0.32 ± 0.45	-0.83 ± 0.35
16 A^f_p (y-cavity)	-1.86 ± 0.87	-0.33 ± 0.49	0.33 ± 0.34	-0.65 ± 0.37
17 A^f_p (E-cavity)	-1.23 ± 0.57	-0.46 ± 0.46	-1.39 ± 1.16	1.00 ± 1.92
18 $\overline{A}_p$ (x, y, E)	-1.51 ± 0.56	-0.18 ± 0.46	0.16 ± 0.34	-0.68 ± 0.35
19 $\overline{A}_C$ (estimator)	2.59 ± 1.52	-4.08 ± 1.55	2.71 ± 1.22	-4.59 ± 1.22
20 $\overline{\overline{A}}_C$ (fitted χ^2)	2.79 ± 1.56	-4.96 ± 1.59	2.81 ± 1.28	-3.88 ± 1.27
21 $\overline{\overline{A}}_{corr}$ (estimator)	$4.10 \pm 1.52 \pm 0.56$	$-3.90 \pm 1.55 \pm 0.46$	$2.55 \pm 1.22 \pm 0.34$	$-3.91 \pm 1.22 \pm 0.35$
22 $\overline{\overline{A}}_{corr}$ (estimator)	$-4.00 \pm 1.09 \pm 0.36$		$-3.23 \pm 0.86 \pm 0.24$	
23 $\overline{\overline{A}}_{corr}$ (estimator)	$-3.5 \pm 0.7 \pm 0.2$			

The symbols are explained in the text. The asymmetries listed have to be multiplied by 10^{-6}.

by the feed-back regulation. Table 1 lists the relevant run data. Note that the asymmetry at the beam intensity monitor in front of the target (A_I) is not necessarily identical with A_e, since variations of the emission of the source are correlated to variations of its phase space. The latter may well compensate or reinforce A_e in the course of acceleration and transport of the beam to the target.

2.3. THE GAS ČERENKOV DETECTOR

At medium electron energies of $E_0 \approx 300$ MeV the total cross section for backward scattering is dominated by the quasi-elastic scattering process around $E' \approx 200$ MeV (see fig. 5). Therefore, this process can be detected efficiently by large solid angle detectors without requiring, in principle, exact energy determination of the scattered electrons or further coincidence conditions, etc.

The detector system chosen consists of 12 ellipsoidal gas Čerenkov counters positioned with axial symmetry around the beam axis (see fig. 6). It covers scattering angles $115° \leqslant \vartheta \leqslant 145°$ over the full azimuth; this corresponds to a solid angle of 20% of 4π. The detector exploits the fact that Čerenkov photons are emitted in a thin medium like air nearly parallel to the particle momentum ($\theta_C = \arccos 1/n\beta_e = 1.4°$ for $\beta_e = 1$). Therefore, the Čerenkov light can be used not
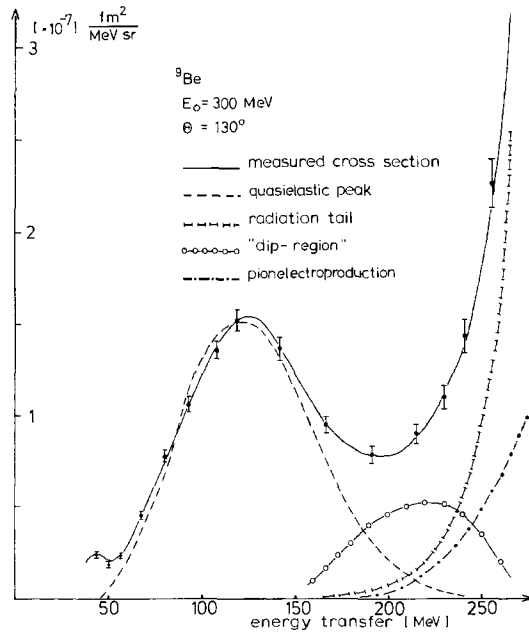

Fig. 5. Spectrum of electrons scattered off ^{9}Be at an angle of 130° as a function of the energy transfer. The beam energy was 300 MeV. Also shown are the spectra of the different scattering processes contributing to the measured cross section.
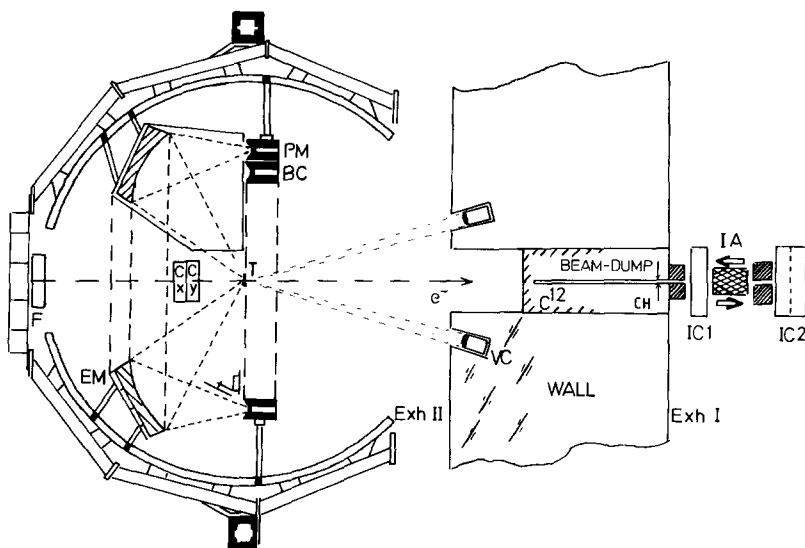
Fig. 6. Side view of the gas Čerenkov detector system and the Compton polarimeter: EM = elliptical mirrors, PM = photomultipliers, BC = background counters, VC = forward angle lucite Čerenkov detectors, T = ^{9}Be target (m_ρ = 2.4 g cm^{-2}), F = ferrite, C_x, C_y = position-sensitive cavities, CH = channel ($\varnothing$ = 1 cm), IC1, IC2 = ionization chambers, IA = magnetized iron absorber.

only for detecting the particle but also for imaging its vertex. The vertex imaging turned out to be an excellent tool for background rejection and subtraction. In the present set-up each of the twelve ellipsoidal mirrors focusses the Čerenkov light onto a separate 2 inch photomultiplier cathode with the target being placed in the other focus. The effective radiator length varies from 74 cm for $\theta = 145°$ to 116 cm for $\theta = 115°$. Another advantage of choosing an air radiator is its high threshold of 25 MeV for electrons. Therefore, large parts of the intense radiation tail at low energies E' are cut off (see fig. 5) as well as the background from any other, heavier particle.

The electron detection efficiency ($T(E', \vartheta, \varphi)$) of these counters, as well as their analog signal height ($\Lambda(E', \vartheta, \varphi)$), were measured as a function of energy and angles in a separate experiment [15]. Fig. 7a shows a contour plot of T and Λ for $E' = 200$ MeV over the surface of the mirror. For the final analysis of the data, the mirrors were divided up into 5 zones of scattering angles ϑ, and average values of T and Λ were evaluated in each zone. In fig. 7b $\overline{\Lambda}(E, \Omega)$ is plotted as a function of energy. Together with the known double differential cross sections the Λ-values enabled a detailed analysis of the composition of the integral analog signal measured (cf. also appendix A).

The photomultipliers were shielded against direct background radiation from the target and the beam dump region by 5 cm of lead. However, they were exposed to

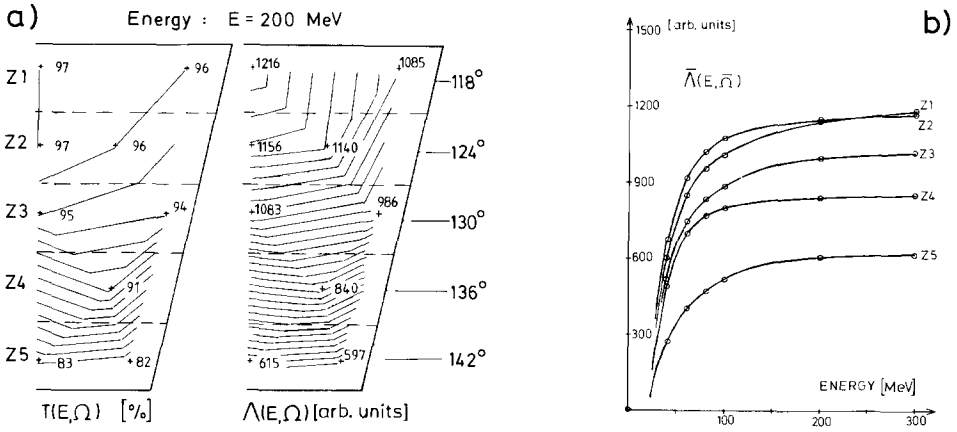a) Energy : E = 200 MeV　　　　　　　　　　b)

Fig. 7. (a) Contour plot of the detection efficiency $T(E, \Omega)$ as well as the analog signal height $\Lambda(E, \Omega)$ over the surface of the Čerenkov mirror for $E = 200$ MeV. The mirrors have trapezoidal boundaries in order to cover fully the scattering angle. Only half of the mirror surface is shown. (b) Average values of $\overline{\Lambda}(E, \Omega)$ evaluated in each of the five zones of the scattering angle ϑ as a function of energy.

the halo background which is produced upstream (e.g. at some diaphragm) and which is travelling along with the beam. In between subruns the signal-to-background ratio could be measured on-line for each detector unit by tilting its mirror by remote control so that the target image was scanned over the photocathode. The corresponding signal is plotted in fig. 8. In focus it reaches a level five times higher than the background. During runs the background was measured simultaneously by
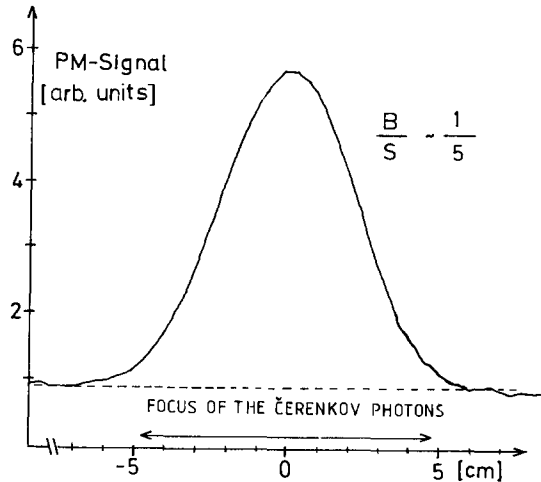

Fig. 8. Focussing properties of the gas Čerenkov detector. Shown is the scan of the focus of the Čerenkov photons across the photocathode ($\varnothing = 50$ mm) by tilting the mirror.

four additional PM units out of focus; they were distributed symmetrically over the azimuth. The origin and nature of the background were further analyzed between subruns by removing the target from the beam and by shutters mounted in front of the twelve photocathodes for the Čerenkov light and the four photocathodes for background detection. Thus it was found that about 1% of the total signal originated from the critical halo background mentioned before.

3. Data taking

For each beam pulse the analog signal of the detectors and beam monitors were integrated in wide-gated ADC's processed by an LSI 11-73 computer and written on tape together with other relevant information on the status of the pulse, see table 2. This procedure provided us with detailed and redundant data which enabled a thorough off-line analysis of the detector response and possible fake asymmetries. When we operated the accelerator with its usual thermionic electron source, i.e. with unpolarized electrons, no significant asymmetry of the apparatus was observed.

TABLE 2
List of the signals of the detectors and of the beam monitors
written on tape for each beam pulse

| Number of signals	Source	Purpose	Symbol (used in the text)	Calculated quantities
12	photomultiplier	gas Čerenkov signal	$S_C = \sum_{i=1}^{12} S_{C,i}$	$A_C = \dfrac{S_C^+ - S_C^-}{S_C^+ + S_C^-}$
4	photomultiplier	background detector	$S_B = \sum_{i=1}^{4} S_{B,i}$	$A_B = \dfrac{S_B^+ - S_B^-}{S_B^+ + S_B^-}$
4	photomultiplier	forward angle counter	–	–
2	ionization chamber (IC_1, IC_2)	Compton polarimeter	$R = \dfrac{IC_2}{IC_1}$	$A_R = \dfrac{R^+ - R^-}{R^+ + R^-}$
1	Rogowski coil	intensity monitor at target position	I	$A_I = \dfrac{I^+ - I^-}{I^+ + I^-}$
1	Rogowski coil	emission current	I_e	$A_e = \dfrac{I_e^+ - I_e^-}{I_e^+ + I_e^-}$
3	microwave cavity	position and energy monitor of the electron beam	x, y, E	$\langle x^+ - x^- \rangle$ $\langle y^+ - y^- \rangle$ $\langle E^+ - E^- \rangle$
1	shot counter	registration	–	–
2	logical level	status of the beam polarization	$+, -$	–
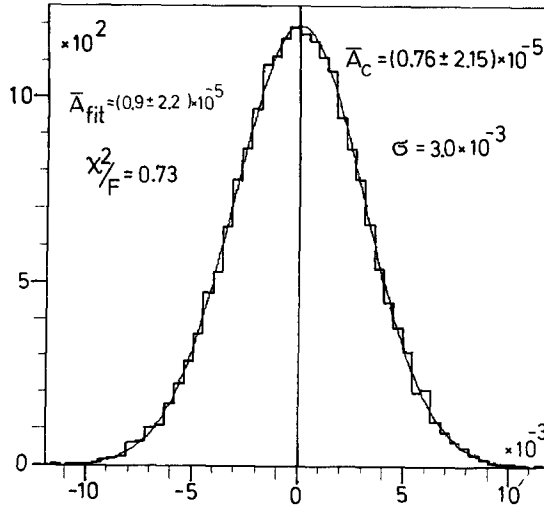
Fig. 9. Histogram of single asymmetries (A'_C) measured with polarized electrons for a 15 min subrun. The solid curve is a gaussian fitted to the measured distribution. The results of the fit $\overline{A}_{fit}$, σ and χ^2/F are given in the figure together with the mean value $\overline{A}_C$ and its error bar.

After several test runs that led to improvements of the apparatus, two final production runs were performed, lasting 100 h and 120 h, respectively. They were divided up into the $\lambda/2^+$ and $\lambda/2^-$ subruns mentioned above. All parameters could be checked on-line. Histograms of signal heights from individual pulses were particularly useful in controlling stable running conditions. After each subrun the histogram of single PV asymmetries and their mean value were calculated and plotted (see fig. 9). Each subrun contains 22 500 pairs (N) of beam pulses. If necessary the source, the accelerator or the beam line were retuned between subruns.

4. Data analysis

4.1. MEASURED ASYMMETRIES AND STATISTICAL CHECKS

Two methods were used to determine the mean value of the asymmetry $\overline{A}_C$ measured by the Čerenkov counters and its standard deviation $\Delta\overline{A}_C = \sigma/\sqrt{N}$, where σ^2 is the variance of the sample of the N single asymmetries of a 15 min subrun:

(i) calculation of the usual estimators

$$\overline{A}_C = \frac{1}{N} \sum_{i=1}^{N} A^i_C; \qquad \sigma^2 = \sum_{i=1}^{N} \left(A^i_C - \overline{A}_C\right)^2 / (N-1); \qquad (5)$$

(ii) fit of the probability function of the normal distribution

$$P(A_C) = P_0 \exp\left\{ -\left(A_C - \bar{A}_C\right)^2 / 2\sigma^2 \right\} \qquad (6)$$

to the measured histogram of single asymmetries by the method of least squares. The result from both methods (fig. 9) agreed well within statistical errors except when the running conditions were disturbed by instabilities which concerned in particular the halo background. Also the χ^2-test of the fit showed satisfactory results.

The variance σ^2 was found to be 10^{-5} typically which agreed well with the expected value

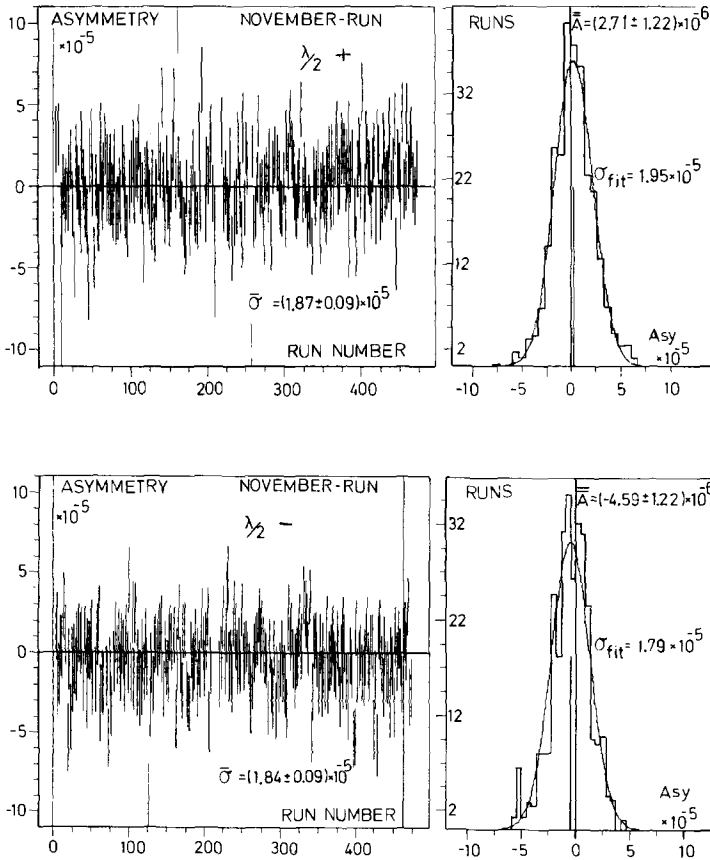$$\sigma^2 = \left(\delta A_C^i / A_C^i\right)^2 = 1/N_i^e, \qquad (7)$$

Fig. 10. (Left) Time sequence of the asymmetries of 15 min runs $\lambda/2^+$ (top) and $\lambda/2^-$ (bottom). The 450 runs correspond to a total beam time of 120 h (run of November 1986). (Right) Histogram of 15 min subrun asymmetries together with the fitted normal distribution.

where N_i^e is the number of electrons scattered into the detector during a single pair of beam pulses. The standard deviation $\sqrt{\sigma^2/N}$ of a subrun asymmetry was about 2×10^{-5}.

Single pair data were rejected whenever the signals described in the following deviated simultaneously by more than 2.5σ from their average: (i) the asymmetry of σ^+-, σ^--beam intensities measured by the ferrite in front of the target, (ii) the sum of the signal heights of the four background counters (S_B). These precautions protected the data from some stray shots way out.

Fig. 10 shows the time sequence of $\overline{A}_C$ obtained from the $\lambda/2^+$- and $\lambda/2^-$-subruns in November 1986 together with their histogram and the fitted average $\overline{A}_C$ and σ_{fit}. These averages are listed separately in lines 19 and 20 of table 1 for the $\lambda/2^+$ and $\lambda/2^-$ runs in May and November 1986. The estimators [eq. (5)] are given as well as the fitted results [eq. (6)]. In all cases the sign and size of $\overline{A}_C$ are correct and distinctly different from zero. All asymmetries given were calculated by normalizing the gas Čerenkov signal to the incoming beam intensity (I) measured in front of the target.

4.2. INVESTIGATION AND CORRECTION OF FAKE ASYMMETRIES

The sources of possible fake asymmetries may be grouped into two categories: (i) purely instrumental ones, (ii) spin-dependent parity conserving processes which may simulate parity violating ones in combination with some instrumental imperfections.

4.2.1. Halo background. Out of the first group the halo background (H) turned out to be the most troublesome since it was correlated to variations of the emission current I_e by a steep slope $(\delta H/H)/(\delta I_e/I_e)$ which could reach a value of 10 in extreme cases. There were no sufficiently safe experimental means to correct the Čerenkov signal for such a fake asymmetry as long as it is as large or even larger than the PV effect. The problem is that the halo background bypassed the intensity monitor in front of the target and hit the PM's directly and hence escaped the normalization. In principle, the signals from the background counters (S_B) might be used for detecting and eliminating the halo asymmetry. But their limited statistical accuracy as well as the uncertainty in the spatial distribution of H did not allow for a substantial correction of this type of background.

On the other hand, the analysis of data revealed a strong correlation of the halo background to any detectable changes in the position and energy of the beam. Since these parameters were measured with high resolution and statistical accuracy by the monitor cavities, they could be used to correct for a residual A_H^f (see below).

The problem was overcome finally by (i) suppressing H as far as possible, i.e. to about 1% of the Čerenkov signal, and (ii) by minimizing the polarization-dependent asymmetry of the beam intensity to a level below 10^{-5} as described in subsect. 2.2. Hence the resulting fake asymmetry due to halo background A_H^f was suppressed to the level of 10^{-7}.

4.2.2. Beam position and energy correlations. As mentioned in subsect. 2.3 the mirrors of the Čerenkov counters image the beam spot on the target onto the photocathodes of the PM's. Since their sensitivity displays local inhomogeneities and since the halo of the diffuse image extends a bit beyond their boundary, the signal S_C will be slightly dependent on the position of the beam spot. Similar considerations concern the energy dependence of S_C, as any shift of the beam energy will cause a change in the inclusive cross section. In addition to these direct dependences of S_C on the beam parameters, an indirect one occurs through the halo background being strongly correlated to the beam parameters, as mentioned above.

Polarization-dependent shifts $(x^+ - x^-)$, $(y^+ - y^-)$ and $(E^+ - E^-)$ of the beam position x, y and energy (E) will therefore cause an average fake asymmetry of the Čerenkov signal given by

$$\langle A_C^f \rangle_{x, y, E} = \frac{1}{2S_C} \left[\frac{\partial S_C}{\partial x} \langle x^+ - x^- \rangle + \frac{\partial S_C}{\partial y} \langle y^+ - y^- \rangle + \frac{\partial S_C}{\partial E} \langle E^+ - E^- \rangle \right]. \quad (8)$$

The derivatives $\partial S_C/\partial x$, $\partial S_C/\partial y$, $\partial S_C/\partial E$ can be determined experimentally from the accidental jitter of the beam position and energy which was more than a factor of 100 larger than the averaged polarization correlated shifts $\langle x^+ - x^- \rangle$, $\langle y^+ - y^- \rangle$, $\langle E^+ - E^- \rangle$ (see table 1). Fig. 11 shows a typical histogram of the jitter of the x-position for a 15 min subrun. For optimized beam steering it was found to be a gaussian. Similar histograms were obtained for the y- and E-jitter.
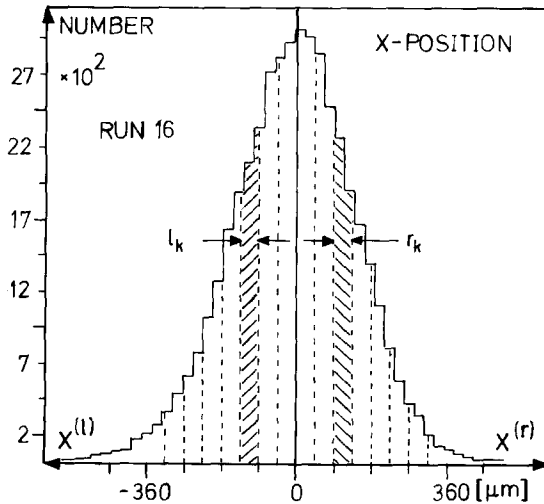

Fig. 11. Typical histogram of the beam jitter in the horizontal x-axis during a 15 min subrun. The intervals to the left (l_k) and to the right (r_k) are used to determine the asymmetry of the detector response with respect to the beam position.
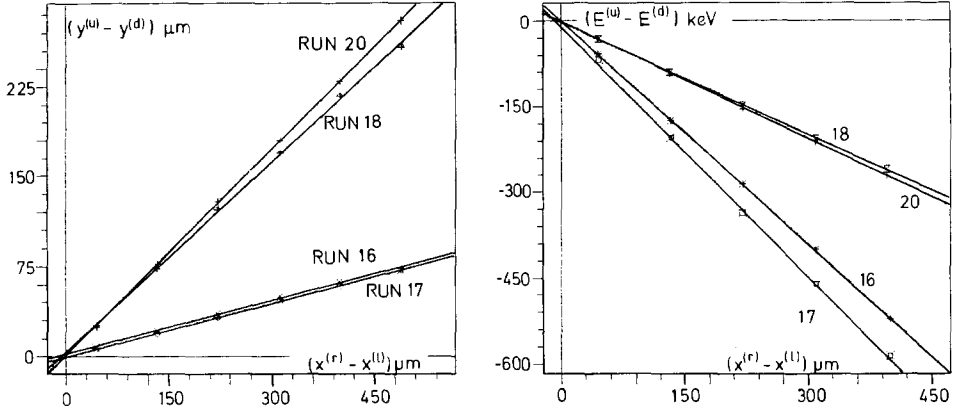
Fig. 12. Examples of the correlations among the beam parameters, position and energy, measured for particular 15 min subruns. The intervals of the y- and E-jitters are obtained from the respective histograms like in fig. 11 with the definitions u (d) for an upshift (downshift) of the beam position or energy.

It turned out, however, that the fluctuations of the different beam monitor signals were strictly correlated to each other. Fig. 12 shows some examples of correlations between x- and y-jitter and x- and E-jitter, obtained for some particular subruns. In between these subruns the beam was occasionally retuned which led to a change of the correlation.

The dependence of S_C on a beam parameter, e.g. the x-position, was derived from the correlation of S_C to the x-jitter in the following way: The x-histogram (fig. 11) is grouped into seven intervals $x^{(l_k)}$ to the left of the average position and seven intervals $x^{(r_k)}$ to the right of it. From the data $S_C^{(l_k)}$, $S_C^{(r_k)}$ obtained within these intervals one calculates asymmetries

$$A^{(k)}_{x\text{-jitter}} = \left(S_C^{(r_k)} - S_C^{(l_k)} \right) / \left(S_C^{(r_k)} + S_C^{(l_k)} \right). \qquad (9)$$

The $A^{(k)}_{x\text{-jitter}}$ are plotted as a function of $\langle x^{(r_k)} - x^{(l_k)} \rangle$ for a particular subrun in fig. 13. The slope of a straight line fitted to the data points would in principle represent the logarithmic, partial derivative $(1/2S_C) \cdot (\partial S_C/\partial x)$ of eq. (8), if, and only if, the jitter of the beam parameters were uncorrelated. Due to the strict correlation of jitters, however, it is already the total logarithmic derivative

$$\frac{1}{2S_C} \frac{dS_C}{dx} = \frac{1}{2S_C} \left[\frac{\partial S_C}{\partial x} + \frac{\partial S_C}{\partial y} \frac{dy}{dx} + \frac{\partial S_C}{\partial E} \frac{dE}{dx} \right] = \frac{dA_{x\text{-jitter}}}{dx}, \qquad (10)$$

where the derivatives dy/dx and dE/dx are given by the slopes of the correlation plots in fig. 12. Therefore, the total fake asymmetry (A^f_P) introduced by polariza-
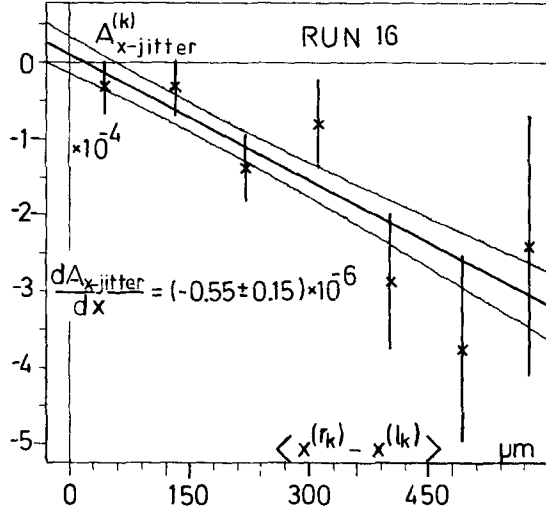
Fig. 13. Asymmetry $A^{(k)}_{x\text{-jitter}}$ of detector response as a function of the shift of the x-position of the beam from the right $(x^{(r_k)})$ to the left $(x^{(l_k)})$ of the average position obtained for subrun 16. From these data the slope $(\mathrm{d}A_{x\text{-jitter}}/\mathrm{d}x)$ is determined which is used to evaluate the helicity-dependent fake asymmetry according eqs. (10) and (11).

tion-dependent shifts of all relevant beam parameters can already be calculated from the correlation diagram of $A^{(k)}_{\text{jitter}}$ with respect to only one of the beam parameters, e.g. the x-position as in fig. 13. Thus we obtain for a particular subrun i

$$A^{f}_{P,i} = \frac{1}{2S_C}\left(\frac{\mathrm{d}S_C}{\mathrm{d}x}\right)_i \langle x^+ - x^- \rangle_i . \tag{11}$$

Typically the logarithmic derivatives in eq. (11) were found to be $10^{-6}/\mu\text{m}$. Since the averaged polarization-dependent shifts $\langle x^+ - x^- \rangle_i$ were about 1 μm, the $A^f_{P,i}$ ranged about 10^{-6} (cf. table 1). They were calculated for each subrun and subtracted from the observed asymmetry $\overline{A}_{C,i}$ in the final analysis. From what was said before, it follows that A^f_P may be evaluated in the same way from an analysis of the y-jitter or the E-jitter. In fact, this was done in order to check the consistency of the procedure. The results agree within their limits of error (see table 1).

4.2.3. Nonlinearities. Assuming that the analog measurement of the Čerenkov signals or of the beam intensity (I) are slightly nonlinear, one may write their ratio as

$$S_c^{\pm}/I^{\pm} = b^{\pm} + cI^{\pm} , \tag{12}$$

where the coefficient c is a measure of the nonlinearity. The normalized asymmetry

A_C now consists of two terms

$$A_C = \frac{S_c^+/I^+ - S_c^-/I^-}{S_c^+/I^+ + S_c^-/I^-} = A_{PV} + A_n^{(f)} \approx \frac{b^+ - b^-}{b^+ + b^-} + \frac{c}{b} I A_I, \tag{13}$$

where in addition to the PV asymmetry (A_{PV}) a fake asymmetry A_n^f is introduced which is proportional to the relative nonlinearity cI/b and the asymmetry A_I of the beam intensity. Since cI/b was found to be smaller than 1% in all cases as long as $I < 20\ \mu$Amp, A_n^f could be safely neglected in view of the small A_I value achieved (see table 1).

4.2.4. Electronic crosstalk. As already mentioned, the switching of the polarization by a Pockels cell requires high voltage levels which could change the bias of the analog detector signals and the recording system by some kind of electronic crosstalk. Although a fake asymmetry due to this effect was eliminated already by turning the $\lambda/2$ plate after each subrun, we checked this effect independently in simulated runs where the detectors were fed by appropriate signals from light diodes instead of Čerenkov light. After careful wiring and grounding of the electronics, no electronic asymmetry was observed within the statistical error limits of 8×10^{-8}.

Fake asymmetries from spin-dependent parity conserving processes could arise from Møller scattering and Mott scattering. The differential cross section for Møller scattering is given by the tensor product [13, 21]

$$d\sigma/d\Omega = (d\sigma/d\Omega)_0 \left(1 + \sum_{i,j} a_{i,j}(\vartheta) P_{i,\text{beam}} P_{j,\text{target}}\right); \qquad i, j = x, y, z \tag{14}$$

in which $P_{i,\text{beam}}$ and $P_{j,\text{target}}$ are the components of the polarization of the beam and target electrons, respectively. Since the detector itself contained no ferromagnetic material, a Møller asymmetry could arise – if at all – only from scattering of halo electrons from the poles of the magnet M_3 in front of the target (see fig. 1). From eq. (14) one derives an asymmetry with respect to the reversal of P_{beam}

$$A_{\text{Møller}} = a_{zx} P_{z,\text{beam}} P_{x,\text{magnet}} \tag{15}$$

with the coefficient [11, 13]

$$a_{zx} \approx -2\sin^2\tilde{\theta}_M \cos\tilde{\theta}_M \Big/ \left[\tilde{\gamma}\left(4 - \sin^2\tilde{\theta}_M\right)^2\right], \tag{16}$$

valid for $\tilde{\gamma} \gg 1$, where $\tilde{\gamma}$ and the scattering angle $\tilde{\theta}_M$ are measured in the c.m. system. For scattering into the detector photomultipliers one calculates $\tilde{\theta}_M \approx 170°$ and $\tilde{\gamma} \approx 17.3$. With $P_{z,\text{beam}} \approx 0.44$ and $P_{x,\text{magnet}} \approx 0.04$ one obtains

$$|A_{\text{Møller}}| \approx 5 \times 10^{-6}.$$

A very conservative upper limit for the contribution of Møller scattering is the "target out" signal which is a factor 60 smaller than the "target in" signal [11]. Hence a fake asymmetry induced by Møller scattering is limited to

$$|A^f_{\text{Møller}}| < 8 \times 10^{-8} \tag{17}$$

and is therefore negligible.

Asymmetry by Mott scattering in the target arises from the transverse component of the beam polarization which was measured by the Møller polarimeter to be smaller than [11,22]

$$P_\perp < P_e \sin 8^0 = 0.06 .$$

The corresponding cross section is given by

$$\frac{d\sigma(\vartheta, \varphi)}{d\Omega} = \left(\frac{d\sigma(\vartheta)}{d\Omega} \right)_{P_\perp = 0} (1 - P_\perp S(\vartheta) \sin \varphi), \tag{18}$$

where the azimuth φ is measured with respect to $P_\perp$. The Sherman function $S(\vartheta)$ may be approximated for energies $E_0 \gg 10$ MeV by [23]

$$S(\vartheta) \approx \frac{4\alpha Z\beta(1/\sin \vartheta)\ln(1/\sin(\vartheta/2))}{\gamma\left[1/\sin^4(\vartheta/2) - \beta^2/\sin^2(\vartheta/2)\right]} . \tag{19}$$

Averaging $S(\vartheta)$ over the dominant processes (quasi-elastic scattering and radiation tail) led to the upper limit [11]

$$\overline{S(\vartheta)}P_\perp < 1.2 \times 10^{-5} .$$

The resulting Mott asymmetry in the sum of the signals of the 12 Čerenkov detectors is, however, strongly suppressed by their axially symmetric arrangement. The relevant deviation from axial symmetry is expressed by the factor

$$f_{\text{axial}} = \sum_{i=1}^{12} S_{\text{C},i} \sin(\varphi_i - \varphi) / \sum_{i=1}^{12} S_{\text{C},i}, \tag{20}$$

where $S_{\text{C},i}$ is the Čerenkov signal of detector i and $\varphi_i = i \cdot 30°$. It was found that f_{axial} did not exceed 3.6×10^{-3} for any choice of φ. Hence a possible fake asymmetry due to Mott scattering is limited to a maximum $|A^f_{\text{Mott}}| \leqslant 4.3 \times 10^{-8}$, which is again negligible.

Nevertheless, we searched for such an effect by calculating the asymmetries $A_i = (S^+_{\text{C},i} - S^-_{\text{C},i})/(S^+_{\text{C},i} + S^-_{\text{C},i})$ measured by each individual detector i and fitting to them simultaneously the three parameter functions

$$F_i = a + b \sin(\varphi_i - \varphi) \tag{21}$$

by the method of least squares. The constant a reproduced the parity violating asymmetry, determined already from the sum signal. The azimuthal coefficient b was found to be $(2.2 \pm 1.6) \times 10^{-6}$ at an azimuth of $\varphi = (7 \pm 31)^0$ with respect to the vertical axis. In the sum of the signals, b is suppressed by the factor f_{axial} of eq. (20) and hence is negligible.

4.3. FINAL EXPERIMENTAL RESULT

The application of the corrections discussed in subsect. 4.2 leads to the corrected asymmetries ($\bar{\bar{A}}_{corr}$) given in the last three lines of table 1. The average over all runs is

$$\bar{\bar{A}}_{corr} = (-3.5 \pm 0.7 \pm 0.2) \times 10^{-6}, \tag{22}$$

where the first error is the statistical and the second the systematic one. From this value we derive the final experimental result (A_{ex}) by eliminating the dependence on technical parameters, namely the background to signal ratio (B/S) and the electron polarization, by the relation

$$A_{ex} = \bar{\bar{A}}_{corr}(1 + B/S)/P_e. \tag{23}$$

Inserting the averaged values $B/S = 0.19$ and $P_e = 44.3\%$ from table 1, we obtain for the parity violating asymmetry in $^9Be(\vec{e}, e')$ scattering at $E_0 = 300$ MeV the value

$$A_{ex} = (-9.4 \pm 1.8 \pm 0.5) \times 10^{-6}. \tag{24}$$

5. Discussion

5.1. EVALUATION OF COUPLING CONSTANTS AND WEINBERG ANGLE

The result (24) may be interpreted in terms of the theoretical expression $\langle A_{qu} \rangle$ for quasi-elastic scattering or, more correctly, in terms of four different scattering processes contributing to the asymmetry (3). Besides the dominant $\langle A_{qu} \rangle$ one has to consider contributions from the electroproduction of pions ($\langle A_\pi \rangle$), from the radiation tail ($\langle A_{rad} \rangle$) and from the "dip region" ($\langle A_{dip} \rangle$), each multiplied with its share η of the measured spectrum (cf. fig. 5):

$$A_{PV} = \eta_{qu}\langle A_{qu} \rangle + \eta_\pi \langle A_\pi \rangle + \eta_{rad}\langle A_{rad} \rangle + \eta_{dip}\langle A_{dip} \rangle. \tag{25}$$

The different contributions have been calculated in appendix A to be

$$\eta_{qu}\langle A_{qu}\rangle = 0.59(2.5\tilde{\alpha} + 1.33\tilde{\gamma} + 2.91\tilde{\beta} + 0.14\tilde{\delta}) \times 10^{-5}, \qquad (26a)$$

$$\eta_{\pi}\langle A_{\pi}\rangle = 0.065(\tilde{\alpha} + 1.8\tilde{\beta})0.92 \times 10^{-5}, \qquad (26b)$$

$$\eta_{rad}\langle A_{rad}\rangle = 0.22(\tilde{\alpha}/8 - (27/8)\tilde{\gamma})(-0.34) \times 10^{-5}, \qquad (26c)$$

$$\eta_{dip}\langle A_{dip}\rangle = 0.125(\tilde{\alpha} + 1.8\tilde{\beta})1.28 \times 10^{-5}. \qquad (26d)$$

Summing up eqs. (26a) to (26d) we obtain eq. (3) which is to be compared with the experimental result (24):

$$(-0.94 \pm 0.18 \pm 0.05) \times 10^{-5} = (1.69\tilde{\alpha} + 2.11\tilde{\beta} + 1.04\tilde{\gamma} + 0.08\tilde{\delta}) \times 10^{-5}. \quad (27)$$

Inserting into eq. (27) the model-independent values for $\tilde{\alpha}$ and $\tilde{\gamma}$ obtained from deep inelastic scattering [7] and atomic spectroscopy [8] (see eq. (2)), one gets the following relation between the two axial vector coupling constants $\tilde{\beta}$ and $\tilde{\delta}$

$$\tilde{\beta} + 0.04\tilde{\delta} = 0.005 \pm 0.17. \qquad (28)$$

The error of this linear combination was obtained by quadratically adding the total relative errors of $\tilde{\alpha}$ and $\tilde{\gamma}$ [eq. (2)] and the total relative error of this experiment [eq. (27)] (arithmetic sum of the statistical and systematic error).

In fig. 14 the result (28) is plotted into the usual diagram of quark coupling constants $C_{2d} = (-\tilde{\beta} + \tilde{\delta})$ and $C_{2u} = (\tilde{\beta} + \tilde{\delta})$ together with the result from the SLAC experiment [7] which was far less sensitive to the axial vector than to the vector coupling constants. The error bar of our result still touches the case of vanishing axial vector interaction ($\tilde{\beta} = \tilde{\delta} = 0$) although it has been improved by a factor of three compared to the previous state of affairs. Also shown is the line predicted by the standard model as a function of $\sin^2\theta_W$. In this case the coupling constants $\tilde{\beta}$ and $\tilde{\delta}$ are replaced by their GWS predictions given in eq. (32). Our result is well centered around the present experimental value of $\sin^2\theta_W$ ($\sin^2\theta_W = 0.223 \pm 0.004$) [4]. That corresponds to

$$\tilde{\beta} = -0.08 \quad \text{and} \quad \tilde{\delta} \equiv 0. \qquad (29)$$

Together with the results from the SLAC experiment which measured a slightly different linear combination of the axial vector coupling constants $\tilde{\beta}$ and $\tilde{\delta}$ [7]

$$\tilde{\beta} + \tfrac{1}{3}\tilde{\delta} = 0.31 \pm 0.51, \qquad (30)$$

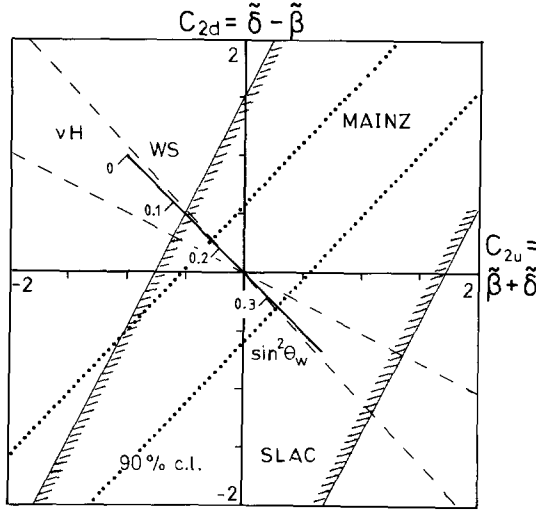one is now able to separate and to determine these constants in a model-indepen-

Fig. 14. Allowed region of the axial vector constants $\tilde{\beta}$ and $\tilde{\delta}$. Dotted lines: this experiment (90% confidence level). Dashed lines: previous SLAC result [7]. In the case of the ν-hadron data (broken lines) factorization is assumed in order to transfer the experimental results to the electron hadron sector [8].

dent way. The result is given in eq. (31)

$$\tilde{\beta} = -0.04 \pm 0.19, \qquad \tilde{\delta} = 1.07 \pm 1.83. \tag{31}$$

A further reduction of the error bars can be obtained by including the results from the neutrino–hadron (νH) scattering experiments [8], also shown in fig. 14. However, the region allowed by a simultaneous fit to the data is model-dependent, as factorization [8] is assumed in order to compare the coupling constants from the νH experiments to the corresponding ones in the electron–hadron sector.

In a model-dependent analysis of our result one replaces the coupling constants in eq. (27) by their GWS prediction [24]

$$\tilde{\alpha} = -\left(1 - 2\sin^2\theta_W\right), \qquad \tilde{\beta} = -\left(1 - 4\sin^2\theta_W\right),$$

$$\tilde{\gamma} = \tfrac{2}{3}\sin^2\theta_W, \qquad\qquad \tilde{\delta} \equiv 0 \tag{32}$$

and obtains for the remaining free parameter, $\sin^2\theta_W$, the value

$$\sin^2\theta_W = 0.221 \pm 0.014 \pm 0.004, \tag{33}$$

where the first error is again due to statistics and the second is the sum of systematic errors.

5.2. NUCLEAR MODEL DEPENDENCE OF THE RESULT

Since our experiment aimed at a model-independent result with respect to weak neutral currents, we will examine in the following whether this result is seriously influenced by model assumptions on the electron–nucleus scattering processes involved. Details are treated in appendices A.1–A.4.

(i) The cross section for the dominating quasi-elastic process is satisfactorily calculated by the assumption of a Fermi gas of nucleons with free nucleon form factors for the electroweak interaction (appendix A.1). Moreover, possible shortcomings of these assumptions mostly cancel in calculating the asymmetry since it depends entirely on the ratio of weak and electromagnetic scattering amplitudes. The conserved vector current, for instance, yields an argument supporting this reasoning.

(ii) In the same way we can conclude that the theory of electroweak production of pions from free nucleons [25] can be transferred to nuclei without introducing a significant model dependence within the present experimental error limits (appendix A.2).

(iii) Electrons in the radiation tail produce a small PV asymmetry by elastic scattering from the nucleus at low energy E' after having emitted bremsstrahlung of energy $E_0 - E'$. A model-independent theory of elastic electroweak scattering from nuclei is given in several papers [26–28]. Therefore, this effect can be taken into account without any serious problems (A.3).

(iv) It is only the dip region for which the insufficient knowledge of the underlying nuclear process introduces a considerable uncertainty in the model-independent representation of the electroweak theory in terms of the coupling constants (appendix A.4). That is the price we had to pay for choosing the highly efficient but inclusive gas Čerenkov detector. Attempts to suppress the dip region (as well as the radiation tail) by a graphite moderator around the target created more problems than they solved, since the signal deteriorated by converting γ's from π^0-decay, bremsstrahlung etc. into e^+, e^- pairs.

The stability of the present result against model errors may be demonstrated by the radical (and unjustified) assumption that the processes competing with the dominant quasi-elastic scattering have zero asymmetry and are therefore treated as spectral background. In this case the analysis would yield for the coupling constants the relation

$$\tilde{\beta} + 0.05\tilde{\delta} = -0.06 \pm 0.19, \tag{34}$$

and for the Weinberg angle the value

$$\sin^2 \theta_W = 0.218 \pm 0.018 \pm 0.005, \tag{35}$$

which are both still compatible with eqs. (28) and (33).

6. Conclusion and outlook

Experimental access to the hadronic axial vector currents in the parity violating, neutral, weak electron–nucleon interaction is less-favoured in comparison to the hadronic vector currents by two facts: (i) the coupling constants $\tilde{\beta}, \tilde{\delta}$ of the former happen to be smaller; (ii) its matrix elements are suppressed in the elastic interaction with heavy nuclei as well as in deep inelastic scattering, to which the previous experiments in atomic and high energy physics were confined. At intermediate energies, however, the sensitivity to $\tilde{\beta}$ and $\tilde{\delta}$ is found sufficiently large to allow these coupling constants to be determined.

This experiment has improved the previous error limits in the sector of $\tilde{\beta}, \tilde{\delta}$ coupling constants by a factor of three. It has largely exhausted the chances offered by inclusive $(\vec{e}, e')$ scattering insofar as the experimental error and the theoretical one which is introduced by the uncertainties in the analysis of the contributions to the inclusive cross section are of same order.

From the physics point of view a further improvement of the precision of the result as well as measurements of other, orthogonal linear combinations of coupling constants would be highly desirable. In the near future the experimental possibilities in this field will be tremendously improved by the forthcoming medium energy cw-electron accelerators at various places which will enable the essential exclusive experiments to be performed with high precision.

Appendix: Spectral components and their asymmetry *

A.1. QUASI-ELASTIC SCATTERING

As already pointed out before and shown in fig. 5 the spectrum of the scattered electrons, detected by the Čerenkov counter, is dominated by the quasi-elastic process, centered at about $E' \approx 200$ MeV and momentum transfer $\langle q \rangle \approx 450$ MeV/c. Integrated over energy and the detector response function it contributes 59% to the total signal. Since $\langle q \rangle$ is more than a factor 2 above the Fermi momentum of the nucleons in ^{9}Be, the quasi-free approximation holds well. Accord-

---

* Details of the following calculations are given in ref. [11].

ing to this the elementary free nucleon cross section has to be folded by the momentum distribution $n_0(k)$ of the bound nucleons [29]. $n_0(k)$ is obtained from harmonic oscillator wave functions, the parameters of which can be drawn from a ^{9}Be$(e, e'p)$ experiment by Frullani et al. [30].

The integral asymmetry due to quasi-elastic scattering can then be written as a folding of functions F_j, containing all kinematical parameters and parameters connected with the apparatus, with the matrix elements $M^{\pm}$ of free eN scattering for + and − electron helicity

$$\langle A \rangle_{\mathrm{qu}} = \frac{\sum_{j=1}^{A} \iiint F_j \left(|M_j^+|^2 - |M_j^-|^2 \right) \mathrm{d}^3 k_j \, \mathrm{d}E' \, \mathrm{d}\Omega}{\sum_{j=1}^{A} \iiint F_j \left(|M_j^+|^2 + |M_j^-|^2 \right) \mathrm{d}^3 k_j \, \mathrm{d}E' \, \mathrm{d}\Omega} . \tag{A.1}$$

The sum is over all nucleons. The functions F_j are

$$F_j = \Lambda(E', \Omega) \frac{E'}{E_0} \left(\frac{m_e}{2\pi} \right)^2 n_{0j}(k_j) \left(1 - n_{0j}(k_j + q) \right)$$

$$\times \delta \left(E_0 - E' - \frac{P_R^2}{2M_{A-1}} - \frac{k_j^2}{2M} - \Delta E_B \right), \tag{A.2}$$

where Λ is the energy- and angle-dependent analog response function of the Čerenkov detector, mentioned in subsect. 2.3. The momentum distribution is chosen to be

$$n_{0j}(k_j) = \left[1 + \tfrac{2}{3}(k_j/P_{0N})^2 \right] \exp \left[-(k_j/P_{0N})^2 \right] \qquad \text{for protons},$$

$$n_{0j}(k_j) = \left[1 + (k_j/P_{0N})^2 \right] \exp \left[-(k_j/P_{0N})^2 \right] \qquad \text{for neutrons}, \tag{A.3}$$

with $P_{0N} = 115$ MeV/c [30]. The average nucleon binding energy in the δ-function of the total energy is chosen to be $\Delta E_B = 17$ MeV [31]. The parity violating matrix element in the numerator of eq. (A.1) has been calculated by Hoffmann and Reya [9] on the basis of the known nucleon form factors [32]

$$\frac{G_M^p}{1 + \mu_p} = \frac{G_M^n}{\mu_n} = \frac{F_2^p}{\mu_p/2M} = \frac{F_2^n}{\mu_n/2M} = \left(1 - q^2/a^2 \right)^{-2}, \qquad a^2 = 0.71 \, (\mathrm{GeV}/c)^2$$

$$\tag{A.4}$$

and effective weak coupling constants g, f. The formula reads

$$|M_j^+|^2 - |M_j^-|^2$$

$$= \frac{2\sqrt{2}\, G_F \pi \alpha}{m_e^2 M^2 q^2} \Big\{ g_A^c g_V^j \big[\big(G_M^j - 2MF_2^j \big)\big(8M^2 \tilde{E}^2 + 4M\tilde{E}q^2 + 2M^2 q^2 \big) + q^4 G_M^j \big]$$

$$- g_A^c f_V^j \big[2MG_M^j - \big(4M^2 - q^2 \big) F_2^j \big] \big(8M^2 \tilde{E}^2 + 4M\tilde{E}q^2 + 2M^2 q^2 \big)$$

$$+ g_V^c g_A^j \big[4M\tilde{E}q^2 + q^4 \big] G_M^j \Big\}, \qquad j = n, p ; \qquad (A.5)$$

with

$$\tilde{E} = E_0 \Big(\sqrt{1 + k_j^2/M^2} - k_j k_0 / E_0 M \Big).$$

The parameters g, f are connected to the conventional $\tilde{\alpha}, \tilde{\beta}, \tilde{\gamma}, \tilde{\delta}$ through the relations:

$$g_A^c g_V^j = \big[\tfrac{1}{4}\tilde{\alpha}\big(G_M^j - G_M^i \big) + \tfrac{3}{4}\tilde{\gamma}\big(G_M^j + G_M^i \big) \big] ,$$

$$g_A^c f_V^j = \big[\tfrac{1}{4}\tilde{\alpha}\big(F_2^j - F_2^i \big) + \tfrac{3}{4}\tilde{\gamma}\big(F_2^j + F_2^i \big) \big] , \qquad (A.6)$$

where $j = p$, $i = n$ or $j = n$, $i = p$,

$$g_V^c g_A^{p(n)} = \tfrac{1}{4}\big((\mp)\tilde{\beta} - 0.6\tilde{\delta} \big) g_{CA},$$

$$g_{CA} = 1.25\big(1 - q^2/a'^2 \big)^{-2}, \qquad a'^2 = 1.0 \,(\text{GeV}/c)^2.$$

The denominator of eq. (A.1) is twice the Rosenbluth matrix element

$$|M_j^+|^2 + |M_j^-|^2 = \frac{4\pi^2 \alpha^2}{m_e^2 M^2 q^4}$$

$$\times \Big\{ \big[\big(G_M^j - 2MF_2^j \big)^2 - \big(F_2^j \big)^2 q^2 \big]\big(8M^2 \tilde{E}^2 + 2M^2 q^2 + 4M\tilde{E}q^2 \big) + \big(G_M^j \big)^2 q^4 \Big\}$$

$$(A.7)$$

where the weak contribution is neglected. Integration of eq. (A.1) leads to eq. (26a) which relates the asymmetry to the coupling constants $\tilde{\alpha}, \tilde{\beta}, \tilde{\gamma}, \tilde{\delta}$ of the parity violating currents. The averaging over the quasi-free kinematics leads to a reduction of the coefficients by about 20% as compared to the case of scattering from free nucleons at rest. Possible changes of the form factors of bound nucleons are not considered here, but they are expected to be small for light nuclei [33].

A.2. PION PRODUCTION

The differential cross section for electro-production of pions is shown in fig. 5. Folded with the response function of the detector it contributes with a percentage $\eta_\pi = 6.5\%$ to the total signal. Since it is dominated by the tail of the Λ-resonance it peaks at $E' \cong 0$. The asymmetry in Δ-production has been calculated by Jones and Petcov and by Nath and Schilcher [25] along the same lines as for elastic eN scattering [9]. At the energies considered, the leading term is approximately given by

$$A_\Delta = \left(-G_F/2\pi\alpha\sqrt{2}\,\right)\left(\tilde{\alpha} + \tilde{\beta}F\left(q^2, E_0\right)\right)q^2. \tag{A.8}$$

Averaged over quasi-free kinematics and the detector response function one obtains

$$\langle A\rangle_\pi \approx \langle A\rangle_\Delta \approx 0.92\left(\tilde{\alpha} + 1.8\tilde{\beta}\right)\times 10^{-5}. \tag{A.9}$$

A.3. RADIATION TAIL

Low-energy electrons at backward angles stem from a second-order process where they first lose energy by bremsstrahlung and are then elastically scattered at low energy in the Coulomb field of the nucleus [34]. The differential cross section of the radiation tail is shown in fig. 5. It was calculated numerically using known formulas and programs for internal and external bremsstrahlung [34], for the nuclear charge distribution of ^{9}Be [35], and for the phase analysis of elastic scattering [36]. The radiation tail is cut off at the Čerenkov threshold $Q = 25$ MeV and contributes above Q with a percentage of $\eta_{rad} = 22\%$ to the total signal. Bremsstrahlung is peaked sharply into the forward direction and transfers a negligible momentum to the nucleus. Hence the Z^0 exchange with the nucleus is highly disfavoured and leads to an asymmetry of order 10^{-10} only. The subsequent elastic scattering has an asymmetry due to the vector currents acting on the nucleus [26]

$$A_V^{el} = \frac{G}{\sqrt{2}\,2\pi\alpha}\left[\tilde{\alpha}\frac{N-Z}{2Z} - \tilde{\gamma}\frac{3(Z+N)}{2Z}\right]q^2. \tag{A.10}$$

Averaged over the measured part of the radiation tail it yields an asymmetry

$$\langle A\rangle_{rad} = 0.34\left(-\tilde{\alpha}/8 + (27/8)\tilde{\gamma}\right)\times 10^{-5}, \tag{A.11}$$

which amounts to $+2 \times 10^{-6}$ when the GWS prediction is inserted. The additional axial vector contribution to the asymmetry in elastic scattering which is due to the unpaired nucleon has been calculated by Fischer-Waetzmann and Scheck for an energy of 300 MeV [27]. At the much smaller energies characteristic for the radiation tail, it can be neglected. Thus we take eq. (A.11) as an upper limit for the correction.

A.4. DIP REGION

The valley between the quasi-elastic peak and the slope of the Δ resonance peak, the so-called "dip region", is filled up by processes which are not well understood (see fig. 5). Its contribution to the total signal is calculated to be $\eta_{dip} = 12.5\%$.

In order to explain the systematic overshoot in the experimental cross section, two mechanisms have been advanced: The first [37] remains within the framework of the quasi-elastic process with the creation of a Δ but introduces a distortion of its wave function by an assumed average potential. The second mechanism [38] exploits the idea of exchange currents and takes account of the two-body nature of the resulting interaction.

Strictly speaking the origin of the "dip region" is not really clear, except that this process is purely isovector in nature and contributes only to the transverse structure function [39, 40]. Therefore, for a model-independent description of its asymmetry in terms of the neutral current coupling parameters, only the coupling to the hadronic isovector currents has to be considered ($\tilde{\alpha}, \tilde{\beta}$ terms). In our analysis, we take as a basis the first mechanism with the creation of a Δ, for which in the approach of the quasi-free Δ production eq. (A.8) holds. Averaged over its spectrum and the detector efficiency the "dip-region" yields an asymmetry

$$\langle A_{dip} \rangle = 1.28 (\tilde{\alpha} + 1.8\tilde{\beta}) \times 10^{-5}. \qquad (A.12)$$

To give a systematic error for the uncertainty in the estimation of $\langle A_{dip} \rangle$, we allow for a deviation of 30%. Inserting the predictions of the WS model for $\sin^2\theta_W = 0.23$ [eq. (32)], one gets

$$\langle \Delta A_{dip} \rangle = 0.26 \times 10^{-5}. \qquad (A.13)$$

References

[1] F.J. Hasert et al., Phys. Lett. B46 (1973) 138
[2] C. Rubbia et al., Rev. Mod. Phys. 57 (1985) 699
[3] S.L. Glashow, Nucl. Phys. 22 (1961) 579;
    S. Weinberg, Phys. Rev. Lett. 19 (1967) 1264; 27 (1971) 1688;
    A. Salam, Rev. Mod. Phys. 52 (1980) 525
[4] C.-A. Piketty, Proc. Int. Conf. on Weak and electromagnetic interactions in nuclei (Springer, Heidelberg, 1986) p. 603
[5] P.Q. Hung and J.J. Sakurai, Ann. Rev. Nucl. Sci. 31 (1981) 375
[6] P.Q. Hung and J.J. Sakurai, Phys. Lett. B63 (1976) 295
[7] C.Y. Prescott et al., Phys. Lett. B77 (1978) 347; B84 (1979) 524
[8] J.E. Kim, P. Langacker, M. Levine and H.H. Williams, Rev. Mod. Phys. 53 (1981) 211;
    M.A. Bouchiat, J. Guena and L. Pottier, Phys. Lett. B134 (1984) 463;
    S.L. Gilbert, M.C. Noecker, R.N. Watts and C.E. Wieman, Phys. Rev. Lett. 55 (1985) 2680
[9] E. Hoffmann and E. Reya, Phys. Rev. D18 (1978) 3230
[10] R.N. Cahn and F.J. Gilman, Phys. Rev. D17 (1978) 1313;
     E.D. Commins and P.H. Bucksbaum, Ann. Rev. Nucl. Part. Sci. 30 (1980) 1
[11] W. Heil, Ph.D. Thesis, Mainz University, FRG (1987)

[12] W. Hartmann et al., Nucl. Instrum. Methods to be submitted

[13] B. Wagner et al., Nucl. Instrum. Methods to be submitted

[14] J. Ahrens et al., Nucl. Instrum. Methods to be submitted

[15] W. Achenbach et al., Nucl. Instrum. Methods to be submitted

[16] D. Conrath, Ph.D. Thesis, Mainz University, FRG (1983) unpublished

[17] B. Mertin, High frequency position monitors, Internal Report MAMI 7/80, Mainz University, FRG (1980)

[18] C.K. Sinclair, Proc. 6th Int. Symp. on High energy spin physics, Marseille, France (1984)

[19] J. Jethwa and F.P. Schäfer, Appl. Phys. 4 (1974) 299

[20] W. Hartmann, Ph.D. Thesis, Mainz University, FRG (1987) unpublished

[21] H. Olsen, Springer Tracts Mod. Phys. 44 (1968) 83;
G.W. Ford and C.J. Mullin, Phys. Rev. 108 (1957) 477

[22] B. Wagner, Ph.D. Thesis, Mainz University, FRG (1986) unpublished

[23] J.W. Motz, H. Olsen and H.W. Koch, Rev. Mod. Phys. 36 (1964) 881

[24] P.H. Bucksbaum and E.D. Commins, Weak interactions of leptons and quarks (Cambridge University Press, Cambridge, 1983)

[25] D.R.T. Jones and S.T. Petcov, Phys. Lett. B91 (1980) 137;
L.M. Nath, K. Schilcher and M. Kretzschmar, Phys. Rev. D25 (1982) 2300

[26] G. Rufa, Nucl. Phys. A384 (1982) 273

[27] M. Fischer-Waetzmann and F. Scheck, Phys. Rev. D21 (1980) 2510

[28] G. Feinberg, Phys. Rev. D12 (1975) 3575

[29] E.J. Moniz, Phys. Rev. 184 (1969) 1154

[30] S. Frullani and J. Mongey, Adv. Nucl. Phys. 14 (1984)

[31] H. Nguyen-Ngoc and J.P. Perez-y-Jorba, Phys. Rev. 136B (1964) 1036

[32] D.H. Perkins, Introduction to high energy physics (Addison-Wesley, New York, 1982)

[33] E. Meziani, Nucl. Phys. A446 (1985) 113c

[34] L.W. Mo and Y.S. Tsai, Rev. Mod. Phys. 41 (1969) 205

[35] H. de Vries, Nuclear charge-density distribution parameters from elastic electron scattering, NIKHEF (1986)

[36] H.G. Andresen, Int. Conf. on Nuclear physics with electromagnetic interactions, Abstracts of contributed papers, Mainz, FRG (1979)

[37] G. Do Dang, Z. Phys. A294 (1980) 377

[38] J.M. Laget, Nucl. Phys. A358 (1981) 275c

[39] T.W. Donnelly, J.W. van Orden, T. de Forest and W.C. Hermans, Phys. Lett. B76 (1978) 393

[40] P. Barreau et al., Nucl. Phys. A358 (1981) 287c